Machine Learning-Assisted Detection of Phosgene and Acetyl Chloride via a Dual-Probe Fluorescent Platform with Differential Reactivity

Jiantong Ding,[a] Yunhui Meng,[a] Lijia Zhang,[a] Xiaobai Li,[a,*] Mengyao Pan,[e] Wenqi Dong,[b] Kun Song,[a] Yongpeng Liu,[c,d,*] Shilong Yang,[b,*] Hongwei Ma[a,b,*]

[a] College of Chemistry, Chemical Engineering and Resource Utilization, Northeast Forestry University, Harbin 150040, China.

[b] Heilongjiang Key Laboratory of Complex Traits and Protein Machines in Organisms, Northeast Forestry University, Harbin 150040, China.

[c] Yusuf Hamied Department of Chemistry, University of Cambridge, Lensfield Road, Cambridge CB2 1EW, UK.

[d] Institute of Applied Physics and Materials Engineering, University of Macau, Avenida da Universidade, Taipa, Macau 999078, China.

[e] School of Fashion and Textiles, The Hong Kong Polytechnic University, Kowloon, Hong Kong 999077, China.

[*] Corresponding authors. E-mail: Xiaobai Li (lixiaobai2008@126.com); Yongpeng Liu (yl862@cam.ac.uk; ypliu@um.edu.mo); Shilong Yang (syang2020@nefu.edu.cn); Hongwei Ma (mahw@nefu.edu.cn).

ABSTRACT: Phosgene and acyl chlorides are highly toxic chemicals that pose serious threats to human health and environmental safety, yet their rapid and reliable detection remains a major challenge due to their high reactivity and environmental interferences. Herein, we report the rational design and synthesis of two donor-π-acceptor (D-π-A) fluorescent probes, **TPA-APPA** and **TPA-HPO**, which incorporate excited state intramolecular proton transfer (ESIPT) and hybridized localized and charge-transfer (HLCT) characteristics. These probes exhibit fast, highly selective, and sensitive responses toward phosgene, with **TPA-APPA** showing distinct fluorescence enhancement and colorimetric changes for both phosgene and acetyl chloride at low detection limits. Benefiting from its excellent photostability, **TPA-APPA** was successfully applied to bioimaging in live cells and zebrafish. Furthermore, by integrating machine learning algorithms, including convolutional neural networks (CNNs) and the Swin Transformer, we developed a ceramic-fiber detection strip capable of intelligent recognition and classification of fluorescence signal variations. This hybrid system achieved high classification accuracy for toxicant vapors, demonstrating the strong potential of coupling advanced fluorescent probes with machine learning for next-generation toxic gas monitoring and bioimaging applications.

Phosgene ($COCl_2$) is one of the earliest and most widely used choking agents, and its high toxicity can cause permanent damage to the lungs.[1] Similarly, another highly hazardous acyl chloride, acetyl chloride (AC), can cause a burning sensation in the eyes even at extremely low concentrations and is lethal at high exposure levels.[2-4] Despite their acute toxicity and associated safety risks, these two compounds continue to be widely used in the production of pesticides, dyes, pharmaceuticals, rubber, and polycarbonates.[5] Given their potential environmental hazards and the risk of misuse, rapid and accurate on-site detection of these acyl chlorides is crucial for safeguarding environmental safety and public health.[6]

Traditional phosgene and acyl chloride detection methods, such as gas chromatography,[7, 8] electrochemical sensors,[9] and high-performance liquid chromatography,[10] are often costly, bulky, and complex to operate, making them unsuitable for rapid on-site testing. In contrast, sensing technologies based on colorimetric and fluorescence analysis demonstrate significant potential for environmental monitoring and bioimaging due to their miniaturized devices, high sensitivity, and visual detection capabilities.[11] In recent years, considerable attention has been given to the critical influence of the excited state properties of fluorescent materials on sensing performance, leading to the development of various fluorescent detection mechanisms. For example, in 2007, Rudkevich et al. pioneered a phosgene detection method based on the fluorescence resonance energy transfer (FRET) mechanism.[12] Zeng et al. developed a single-molecule probe BDP-CHD that reacts with phosgene to form an octahydrobenzimidazolone-BODIPY structure, yielding bright green fluorescence, while acyl chlorides and DCP convert its amines into amide and phosphamide groups to inhibit photoinduced electron transfer (PET) and produce strong blue fluorescence,

thereby enabling a portable high-throughput fluorescent platform for rapid screening of toxic phosgene, DCP and volatile acyl chlorides.[13] Fang et al. constructed a ratiometric fluorescent probe NPT-HBT that undergoes a rapid cyclization reaction with phosgene to form a benzimidazolone structure, which blocks the intramolecular charge transfer (ICT) process of HBT, thereby shifting the emission from yellow to blue to achieve effective detection and identification of phosgene from interfering substances.[14] Yoon et al. pioneered the incorporation of the excited state intramolecular proton transfer (ESIPT) process in 2017.[15] By leveraging its proton-environment stability and unique emission characteristics, this approach effectively mitigates signal interference caused by nitrogen protonation, significantly enhances detection contrast, and enables dual channel colorimetric fluorescence phosgene detection. However, most existing probes remain susceptible to proton acid interference, as nitrogen containing sites are easily protonated, which weakens their nucleophilicity toward acyl chlorides and perturbs the photophysical properties of the fluorophore, leading to signal drift or quenching. These issues significantly compromise the selectivity and stability of current sensors in acidic conditions.[16] In our previous work, we discovered that fluorescent materials possessing hybridized localized and charge-transfer (HLCT) excited states exhibit outstanding detection performance, high sensitivity, and tunable selectivity.[17] HLCT character can be modulated by structural modification of donor and acceptor units and by altering conjugation, enabling a quantitative investigation of how excited state properties influence sensing metrics.[18] This novel detection mechanism is also considered a promising strategy for designing fluorescent molecular probes.[19]

Herein, we designed and synthesized two ESIPT-HLCT probes, **TPA-APPA** and **TPA-HPO** (**Scheme 1**). Their quasi-rigid D-π-A structures, formed by linking triphenylamine to 2-aminophenyl or 2-hydroxyphenyl via a pyridine bridge, enable orbital mixing and generate HLCT excited states.[20, 21] The ESIPT process further induces enol–keto tautomerism, leading to multiband, wavelength tunable emission with enhanced ratiometric sensing performance. TPA donor suppresses π–π stacking, improving luminous efficiency, while its strong push–pull effect activates recognition sites for rapid acylation by phosgene or acyl chlorides. Consequently, the probes exhibit high sensitivity, fast response, and pronounced fluorescence and color changes.[22] **TPA-APPA** also shows good cell permeability, low cytotoxicity, and excellent biocompatibility in cellular and zebrafish assays. Furthermore, ceramic fiber strips loaded with **TPA-APPA** provide portable visual detection, and integration with Swin Transformer–based image recognition enables intelligent, quantitative classification of toxic gases (**Scheme 1**). This work not only advances hazardous gas sensing but also highlights the broad potential of ESIPT–HLCT mechanisms in next generation optical sensors.

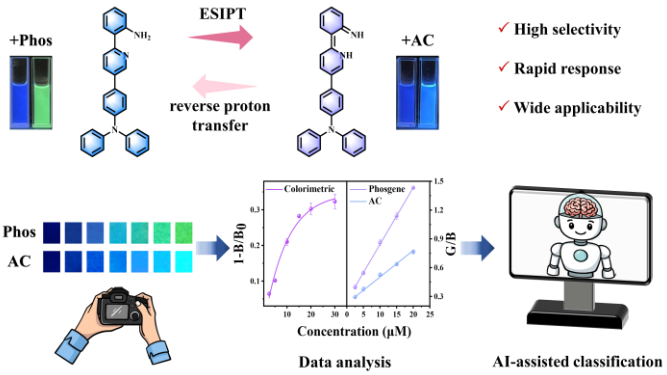

Scheme 1. Detection Mechanism of the HLCT-ESIPT Probe for Phosgene and Acetyl Chloride.

EXPERIMENTAL SECTION

Materials and General Methods. All reagents were purchased from Sigma-Aldrich and utilized without further purification. ^{1}H and ^{13}C NMR spectra were recorded on a Bruker AVANCE III HD spectrometer operating at 500 MHz. MALDI-TOF-MS spectra were acquired using an AXIMA-CFR^{TM} plus instrument. UV-Vis absorption and fluorescence spectra were measured with a TU-1901 spectrometer and an FL-4500 fluorometer, respectively. Additionally, fluorescence spectra were recorded using a Shimadzu RF-6000. Fluorescence decay and photoluminescence quantum yield (Φ) assays were executed on an Edinburgh FLS1000 fluorescence spectrometer. The fluorescence lifetimes (τ) were acquired using a 365 nm laser to excite the samples.

All theoretical calculations were performed using Gaussian 09. The geometries of TPA-APPA, TPA-HPO, and their respective reaction products were optimized at the B3LYP/6-31G(d,p) level. Subsequently, time-dependent density functional theory (TD-DFT) calculations of the excited states were performed with the M06-2X functional.

Synthesis of Chemosensor. TPA-APPA and TPA-HPO were synthesized and purified using available methods,[23, 24] and the details of the synthesis are shown in Figures S1-S6.

Solution Detection. To avoid direct exposure to phosgene, triphosgene was employed to decompose into 3.0 equiv of phosgene in situ in the presence of triethylamine (TEA). Spectroscopic measurements were conducted in a tetrahydrofuran (THF)/TEA (100:1, v/v) mixed solvent.[25-28] Initial samples were prepared by transferring 3 mL of THF/TEA solutions containing probes **TPA-APPA** and **TPA-HPO** (each 5 μM) into cuvettes. Triphosgene at varying concentrations was then added to both initial samples, and the corresponding changes in fluorescence and absorbance spectra were recorded under 365 nm excitation.

Detection of Exogenous Phosgene in Zebrafish. Zebrafish embryos were seeded in 90 mm Petri dishes and cultured in E3 embryo media at 28.5℃. Three-day-old zebrafish larvae were incubated with 5 μM TPA-APPA in E3 embryo media for 0.5 h. Because phosgene is highly toxic and undergoes rapid hydrolysis in aqueous PBS, triphosgene, a solid phosgene-releasing reagent, was used as a safer surrogate to generate exogenous phosgene in vivo. After pretreatment, the zebrafish larvae were incubated with 15 μM triphosgene solution predissolved in PBS for 30 min. After washing with PBS, the zebrafish larvae were anesthetized and euthanized by immersion in 1000 mg L^{-1} MS-222. Images were acquired using a Leica macro fluorescence imaging system equipped with an M205 FCA objective. Raw

images were processed using the instrument's built-in THUNDER mode to reduce background noise and enhance image clarity.[29]

Preparation of Test Strips Loaded. 625 mg of polyethylene oxide (PEO) and 0.01 mmol of **TPA-APPA** were completely dissolved in 50 mL of acetonitrile to form a clear, homogeneous solution.[30] Subsequently, the three materials: non-fluorescent filter paper, meltblown cloth and ceramic fiber, were each cut into 1.5×2.5 cm strips, and the cut substrates were each immersed in this solution for 10 min and placed in a fume hood to dry naturally.

Detection of Phosgene Gas and Other Analytes at Various Concentrations. Seven triphosgene solutions in dichloromethane (DCM) were prepared at concentrations of 0, 0.0125, 0.025, 0.05, 0.075, 0.1 and 0.15 g L^{-1}. Firstly, taking seven 25 mL glass vials, above solutions 20 μL were removed into the bottom of the flasks, followed by the addition of 0.1 equiv TEA in DCM (20 μL), and then quickly closing the lid, respectively. After 5 min, the test strips were introduced into the vials. After 2 min, the test strips were removed from the vials.[31, 32]As a representative example, 20 μL of a 0.4 g L^{-1} triphosgene solution was added to a 25 mL glass vial, followed by 20 μL of a 0.05 mM TEA solution in DCM. The concentration of phosgene gas in the vial was calculated to be 120 mg m^{-3} (30 ppm), assuming complete decomposition of triphosgene to gaseous phosgene (Table S1).

Solutions of the analytes triphosgene, Tosyl chloride (TsCl), $SOCl_2$, AC, Oxalyl chloride (OC), Benzoyl chloride (BzCl), Phosphorus oxychloride ($POCl_3$), formaldehyde (FA), Benzaldehyde (Ben), Diethyl chlorophosphate (DCP), Diethyl Phosphorocyanidate (DCNP), and 2-Chloroethyl ethyl sulfide (CEES) were prepared in DCM (Table S2).[33] An aliquot (20 μL) of each solution was transferred to a separate 25 mL glass vial. Assuming complete vaporization of the analyte, its concentration in the vial headspace was calculated to be 30 ppm. After the test, residual triphosgene and reactive different interferents were chemically quenched with ethanol prior to disposal. The resulting waste was collected and treated as halogenated organic waste in accordance with institutional safety protocols.

RESULTS AND DISCUSSION

Optical Properties of TPA-Based D-π-A Fluorescent Probes. To evaluate the fundamental photophysical characteristics of **TPA-HPO** and **TPA-APPA**, their UV-Vis absorption and photoluminescence spectra were recorded in THF (Figure 1a). The excitation processes of both compounds are concentrated in the conjugated backbone, and the end groups (-NH_2 and -OH) exert negligible influence on the absorption profile, resulting in nearly identical maximum absorption wavelengths at 365 nm. Upon excitation, **TPA-HPO** and **TPA-APPA** emit blue fluorescence centered at 429 nm and 440 nm, respectively. This is because the electrons in **TPA-APPA** are promoted from the donor group toward the extended π system. The resulting spatial separation between the excited electron and the initial hole enhances the intramolecular charge transfer effect, leading to the slightly red shifted emission.

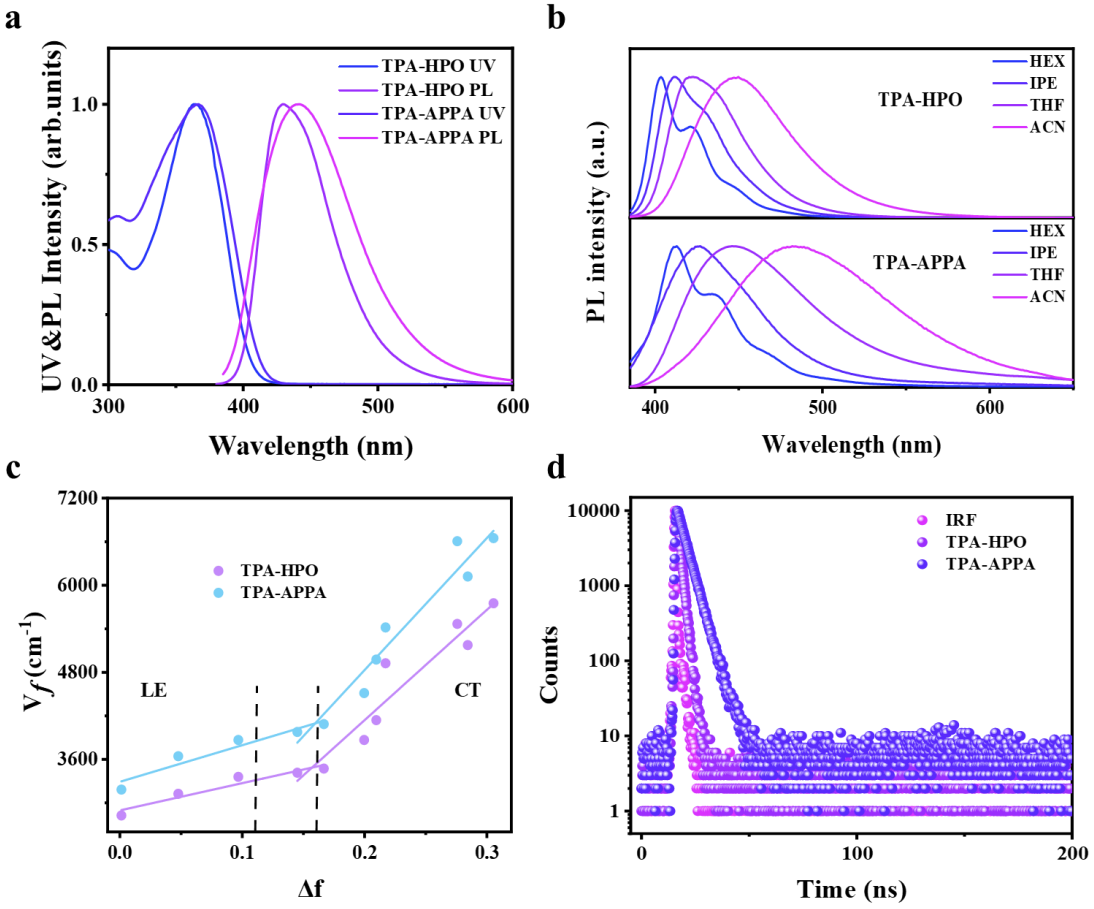

Figure 1. (a) The UV-Vis and PL spectra of **TPA-HPO** and **TPA-APPA** in THF. (b) The solvatochromic effects of **TPA-HPO** and **TPA-APPA** in the increasing polarity solvent. (c) Solvatochromic Lippert-Mataga models of **TPA-HPO** and **TPA-APPA**. (d) Transient photoluminescence spectra of **TPA-HPO** and **TPA-APPA** in THF solution.

By recording the absorption and emission spectra of both probes in various solvents, we observed that the emission wavelengths of the luminophores in both probes exhibited a red shift with increasing solvent polarity, indicating the presence of a CT component in the first excited singlet (S_1) state (Figure 1b). Both probes share the same electron donor triphenylamine moiety and an extended conjugation system, which contributes significantly to the CT state, leading to broadened emission bands and a pronounced solvatochromic response.[34] To quantitatively analyze these effects simultaneously, we established a correlation between the Stokes shift and solvent polarity using the Lippert-Mataga solvent model (Figure 1c).[35] Both probes show dominant local excitation (LE) character in low polarity solvents, while CT contributions become progressively stronger in high polarity solvents. Based on the slopes of the linear fits, the change in excited state dipole moment ($\Delta\mu=\mu_e-\mu_g$) is 9.2 D in low polarity environments and 17.6 D in high polarity environments. In moderately polar solvents (Δ_f=0.12-0.16), the energetic proximity and coupling between the LE and CT states facilitate the formation of the HLCT state, where LE and CT characters are simultaneously involved in the emissive process. The HLCT states were confirmed using time resolved photoluminescence measurements. Transient emission studies in THF revealed exclusively nanosecond scale decay components for both probes, with no evidence of longer-lived processes (Figure 1d). The lifetimes (τ) of **TPA-HPO** and **TPA-APPA** were 1.32 ns and 3.97 ns, respectively. The significantly longer lifetime of TPA-APPA suggests a reduced nonradiative decay rate of its excited state with pronounced CT character. This observation is consistent with the stronger donor strength of TPA-APPA, which is further supported by DFT calculations presented later. Collectively, these results confirm the HLCT state characteristics of the luminophores, where the coexistence of localized and charge transfer excited states enables efficient radiative recombination without triplet state involvement, thereby confirming the synergistic contributions of ESIPT and HLCT mechanisms to the excited state dynamics.

Effect of HLCT-ESIPT on Phosgene and Acetyl chloride Detection Performance. We first investigated the UV-Vis absorption and fluorescence spectral responses of **TPA-APPA** and **TPA-HPO** toward phosgene in THF. The sensing behavior of both probes toward phosgene was evaluated using the solid phosgene equivalent triphosgene, which generates phosgene in situ in the presence of TEA. The **TPA-APPA** probe exhibited a distinct absorption band at 360 nm. Upon addition of phosgene (0-70 μM) and TEA, the initial absorption peak at 360 nm diminished, while a new peak emerged at 440 nm (Figure S7a). This shift was accompanied by a color change from colorless to pale yellow, indicating a structural transformation and formation of a new compound. In terms of fluorescence, the THF solution of **TPA-APPA** emits blue fluorescence at 440 nm. Upon adding triphosgene and TEA to the **TPA-APPA** solution, a new emission peak appeared at 512 nm, changing the fluorescence color from blue to bright green. This shift is attributed to the rapid reaction between the ortho amino group and phosgene, acylation of the ortho-amino substituent inhibits ESIPT, thereby suppressing the probe's HLCT character and enhancing CT character. The result is increased CT contribution and a red shifted emission. This inhibition of the proton transfer route in the excited state induces a transition from a HLCT state to a more CT state. Furthermore, this acylation process enhances molecular conjugation rigidity, effectively increasing the extent of excited state charge transfer. Consequently, this induces a red shift in the emission wavelength, resulting in a visible change in fluorescence color (Figure 2a). The total fluorescence intensity of **TPA-APPA** rapidly increased upon addition of triphosgene and TEA and reached a stable state within 80 s (Figure S9a). It remained stable for at least 60 min at 25°C (Figure S10a), demonstrating excellent response speed and photostability. Over the range of 10-70 μM, the fluorescence intensity ratio I_{512}/I_{440} showed an excellent linear correlation with phosgene concentration (R^2=0.999). Using the equation of the detection limit (LOD), the LOD for phosgene was determined to be 5.2 nM, providing sufficient sensitivity for detection of trace phosgene relevant to industrial leak scenarios and the environment (Figure 2d).

Under identical experimental conditions, the THF solution of **TPA-HPO** exhibits blue fluorescence with an emission peak at 430 nm. This emission is attributed to the formation of a stable hydrogen bond network between the ortho hydroxy group and pyridine, coupled with the induction by the D-π-A structure, which collectively enhances the fluorescence properties of the probe. Upon addition of triphosgene (0-70 μM) and TEA, the **TPA-HPO** probe solution exhibited no noticeable color change (Figure S8). However, fluorescence emission was quenched with increasing phosgene concentration (Figure 2c). This quenching occurs because the ortho-positioned hydroxyl group rapidly undergoes nucleophilic addition, leading to the formation of an aryl chloroformate structure, which disrupts the hydrogen bonding network essential for ESIPT and impedes efficient proton transfer in the excited state. Furthermore, suppression of ESIPT reduces the contribution of the LE component in the HLCT state, resulting in a shift toward a more ICT character in the excited state. This shift increases the delocalization of excited state electrons, promotes none radiative decay pathways, and ultimately leads to substantial fluorescence quenching. Kinetically, the fluorescence intensity of **TPA-HPO** reaches a steady state within approximately 120 s of triphosgene addition (Figure S9b) and demonstrates long term photostability under ambient conditions (Figure S10b). Quantitative analysis reveals a strong linear correlation between the fluorescence intensity of **TPA-HPO** and phosgene concentration up to 70 μM (R^2=0.993). The LOD for phosgene was calculated to be 13.49 nM (Figure 2f), demonstrating that while **TPA-HPO** is less sensitive than **TPA-APPA** for phosgene detection, it retains trace detection capability and is suitable for early warning in high concentration leakage scenarios. Furthermore, to evaluate the response characteristics and spectral behavior of the **TPA-APPA** probe toward AC, its absorption spectrum remained almost unchanged upon AC addition (Figure S7b), in contrast to the response observed with triphosgene. However, fluorescence at 440 nm increased significantly, exhibiting a typical "off-on" fluorescence response (Figure 2b). This phenomenon is attributed to the acylation reaction between the amino group in the molecule and AC, leading to the formation of an amide structure. This modification alters the excited state conformation and electron distribution, thereby promoting radiative transition pathways in the HLCT state. Within the concentration range of 10-70 μM, the fluorescence intensity of **TPA-APPA** showed a strong linear correlation with AC concentration, with

a detection limit of 7.7 nM (Figure 2e). These results confirm that **TPA-APPA** can serve as a sensitive fluorescent sensor for detecting AC.

Selectivity is a critical parameter for assessing the performance of fluorescent probes in analyte detection. To further evaluate this property, the fluorescence responses of **TPA-APPA** and **TPA-HPO** were tested against phosgene, Tosyl chloride (TsCl), $SOCl_2$, AC, Oxalyl chloride (OC), Benzoyl chloride (BzCl), Phosphorus oxychloride ($POCl_3$), formaldehyde (FA), Benzaldehyde (Ben), Diethyl chlorophosphate (DCP), Diethyl Phosphorocyanidate (DCNP), and 2-Chloroethyl ethyl sulfide (CEES). As shown in Figure 2g, phosgene, $SOCl_2$, OC, and $POCl_3$ produced new absorption peaks at 360 nm and 445 nm, accompanied by a color change of the solution from colorless to light yellow (Figure S11).

For TPA-APPA, phosgene, $SOCl_2$, OC, and $POCl_3$ trigger the emergence of new absorption peaks at 440 nm, accompanied by color changes from transparent to pale yellow under daylight. only phosgene induces the decrease of the pristine emission peak at the emission from the 440 nm and dramatic fluorescence enhancement at the 512 nm, whereas AC and OC only enhance the original blue emission with negligible shift of the maximum wavelength (Figure 2h and Figure S12). The remaining acyl chlorides either yield almost no change in the emission spectrum or lead to fluorescence quenching. Therefore, although certain reactive chlorides also induce spectral changes, phosgene can still be readily distinguished by its characteristic red-shifted emission and much larger fluorescence response.

It should be noted that acetyl chloride, as a mono-acyl chloride, is much less reactive than phosgene under the aqueous sensing conditions and is also prone to rapid hydrolysis. Consequently, it cannot efficiently acylate the HPO unit or induce a significant perturbation of the conjugated system of TPA-HPO. Consistently, no new absorption bands are observed for TPA-HPO in the presence of highly chlorinating reagents such as $SOCl_2$, OC, and $POCl_3$ (Figure 2j). In contrast, phosgene triggers pronounced fluorescence quenching at 430 nm (Figure 2k), whereas other potential interferents, including acetyl chloride and related reactive chlorides, cause only negligible or minor changes in fluorescence intensity (Figures 2l and S13).

These results indicate that although the underlying acylation mechanism is similar, the substantially higher electrophilicity and stability of phosgene under the sensing conditions enable efficient interaction with the TPA-HPO unit, thereby giving rise to a distinct optical response. As a result, TPA-HPO exhibits a highly selective fluorescence response toward phosgene over other reactive chlorides.

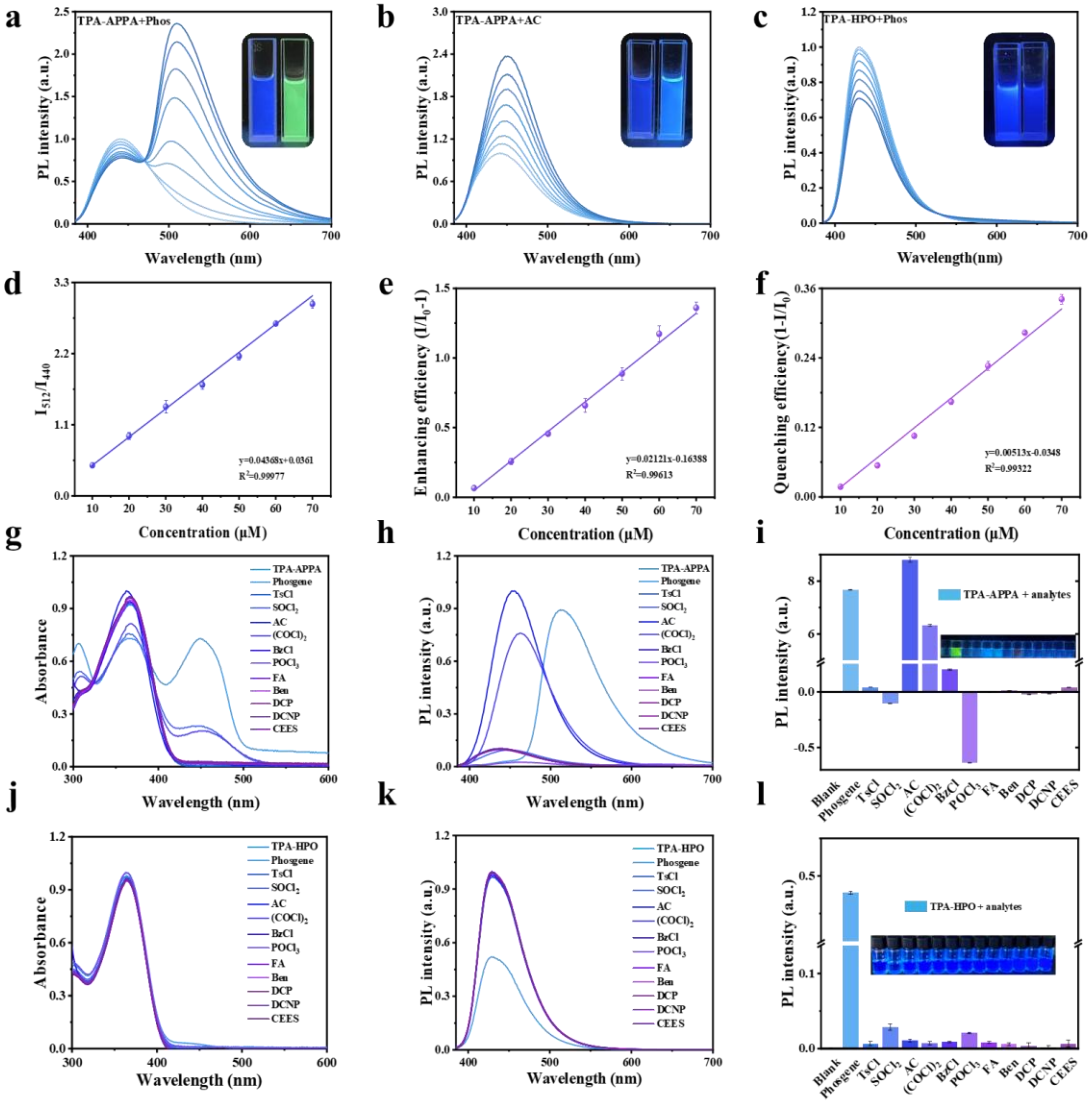

Figure 2. (a, b) Fluorescence spectra of **TPA-APPA** in THF solution with increasing concentrations of phosgene and AC (0-70 μM). The insets show photographs of **TPA-APPA** under 365 nm UV light before and after the addition of phosgene at 24℃ and 30% relative humidity. (c) Fluorescence spectra of **TPA-HPO** in THF solution with increasing concentrations of phosgene (0-70 μM). The inset shows photographs of **TPA-HPO** under 365 nm UV light before and after the addition of phosgene at 24℃ and 30% relative humidity. (d) **TPA-APPA** solution exhibits a linear relationship between the fluorescence intensity ratio (I_{512}/I_{440}) and phosgene concentration. (e) Linear relationship between fluorescence intensity and AC concentration in **TPA-APPA** solution. (f) Linear relationship between fluorescence quenching efficiency of **TPA-HPO** solution and phosgene concentration, with error bars representing the standard deviation (n=3). (g, h, i) UV absorption spectra, fluorescence spectra of **TPA-APPA** solution (5 μM) after addition of phosgene and different interferences (50 μM) at 24℃ and 30% relative humidity, and corresponding fluorescence ratio plots. (j, k, l) Corresponding UV absorption and fluorescence spectra of **TPA-HPO** solution (5 μM) after addition of phosgene and different interferences (50 μM) at 24℃ and 30% relative humidity. Insets show photographs of the respective solutions under 365 nm UV light.

Mechanism Research. Both molecules adopt a D-π-A structural framework bridged by pyridine units, which promotes efficient π-conjugation and spatial separation of frontier molecular orbitals. The incorporation of hydroxyl or amino groups adjacent to the pyridine nitrogen atom enables intramolecular hydrogen bonding, thereby facilitating proton transfer in the excited state.[36] Concurrently, the inherent molecule architecture facilitates HLCT excited state generation while regulating the spatial distribution and overlap between HOMO and LUMO orbitals, thereby determining the excited state dynamics and fluorescence characteristics of the molecules. As shown in Figure 3a, **TPA-APPA** exhibits typical ESIPT behavior, characterized by reversible proton transfer between the amino group and the pyridine nitrogen atom. Given the strong nucleophilicity of the NH_2 group, **TPA-APPA** undergoes amide formation upon treatment with phosgene and acyl chloride, yielding the cyclic adduct **APPA+Phos** and the amide product **APPA+AC**, respectively. To verify that the observed color and fluorescence changes are indeed caused by these two products, we conducted ^1H and ^{13}C NMR titration experiments. The results revealed that the chemical shift signals at 8.88 ppm, 7.91 ppm, 7.29 ppm, 6.78 ppm, 7.06 ppm, and 5.90 ppm in **TPA-APPA** corresponded to protons 1 through 6, respectively. Upon addition of phosgene, the amino proton signal at position 1 completely disappeared, while the resonances at positions 5′, 2′, and 3′ shifted downfield to 8.08, 7.57, and 7.38 ppm, respectively, consistent with the formation of **APPA+Phos** bearing the expected carbonyl functionality. High-resolution mass spectra further confirmed the structure of **APPA+Phos**. The calculated m/z value for **APPA+Phos** agreed well with the LC-ESI-HRMS m/z: found for $[M+H]^+$ 439.94 (Figures S14 and S15). Upon addition of AC, the NH_2 signal at position shifted to 9.92 ppm. Adjacent protons at positions 2″-6″ exhibited pronounced downfield shifts, and a new resonance at 2.2 ppm appeared in the aliphatic region, consistent with the formation of the acetamide structure of **APPA+AC**. These results confirm that acyl chloride binds to the aromatic amino group, producing a pronounced fluorescence enhancement in the blue channel. The calculated mass of the product **APPA+AC** is 454.56, while the measured mass is 455.95, further supporting the accurate validation of the sensing mechanism between probe **TPA-APPA** and acyl chloride (Figure S16). Additionally, fluorescence lifetime decay curves of TPA-APPA were recorded before and after exposure to phosgene, and the fluorescence lifetime shows a single-exponential decay, with an initial lifetime that decreases to an amplitude-weighted average lifetime of 2.13 ns upon exposure to phosgene triggered intramolecular charge transfer (Figure S19a). Furthermore, exposure to phosgene significantly increased the fluorescence quantum yield, from 3.06% to 25.9%. These results suggest that phosgene treatment redirects the excited-state deactivation pathway towards radiative decay, which accounts for the substantial increase in emission efficiency, even though the fluorescence lifetime is reduced.

TPA-HPO exhibits reversible proton transfer between the hydroxyl and pyridine nitrogen. Upon addition of phosgene, the hydroxyl proton undergoes substitution to yield an amide product (Figure 3b). In contrast to the highly nucleophilic amino group in TPA-APPA, this quenching behavior can be rationalized by considering the reaction between the HPO unit and phosgene. The OH group in HPO reacts with phosgene to give a more electron-deficient chloroformate, which both disturbs the π-conjugation and strengthens the acceptor character of the molecule. The resulting product exhibits a more pronounced ICT character and allows an efficient photoinduced electron transfer from the triphenylamine donor to the newly formed electron-deficient center, thus promoting non-radiative decay of the excited state and causing fluorescence quenching of **HPO+Phos** relative to **TPA-HPO**. This was verified via ^1H NMR titration experiments (Figure 3d). The results indicate that the chemical shifts at 14.26, 7.86, 7.35, 7.05, and 6.90 ppm correspond to the proton signals at positions 9 to 12 in **TPA-HPO**, respectively. Upon addition of phosgene, the hydroxyl peak originally at position 14.26 ppm completely disappeared, while the proton resonance signals at positions 9′ to 12′ remained largely unchanged. The product **HPO+Phos** was detected by LC-ESI-HRMS in positive-ion mode, giving an ion at m/z 473.23 corresponding to $[M+H]^+$ (Figure S17 and S18). Additionally, we also collected the fluorescence decay curves of TPA-HPO before and after adding phosgene, and the fluorescence lifetime remained essentially unchanged within experimental uncertainty (Figure S19b). Furthermore, the incorporation of phosgene leads to a decreased fluorescence quantum yield of TPA-HPO from 14.3% to 3.7%. The divergence between Φ and τ strongly argues against dynamic quenching as the dominant pathway. The reduced Φ with nearly constant τ indicates a pronounced suppression of the radiative rate constant accompanied by a compensatory increase in the non-radiative rate constant. The emission attenuation observed upon conversion of TPA-HPO to HPO-Phos may therefore arise from consistent with static quenching. Thereby validating the proposed reaction mechanism of **TPA-HPO**.

To comprehensively investigate the recognition mechanisms of **TPA-APPA** and **TPA-HPO** toward phosgene and AC, as well as their optical sensing response processes, a series of quantum chemical calculations were carried out using the Gaussian 09, Multiwfn, and VMD. Potential energy profiles for **TPA-APPA** and **TPA-HPO** in the S_0 and S_1 states were generated by systematically varying the N-H and O-H bond distances (Figure S20). The calculated energy barriers in the S_0 state were 28.20 kcal mol^{-1} for **TPA-APPA** and 18.62 kcal mol^{-1} for **TPA-HPO**, both higher than the corresponding values in the S1 state. This observation suggests that the ESIPT processes of **TPA-APPA** and **TPA-HPO** are facilitated under photoexcitation. To more

intuitively characterize the weak interactions preceding N-H and O-H bond formation, independent gradient model Hirshfeld (IGMH) isosurfaces were generated using the Multiwfn program (Figure S21).[37] The locations of the blue spikes correspond to the strengths of hydrogen bonding, thereby providing a clearer visualization of changes in hydrogen bond strength. Collectively, these results substantiate the proton transfer processes of the two probes, confirming the presence of essential conditions that enable rapid detection.

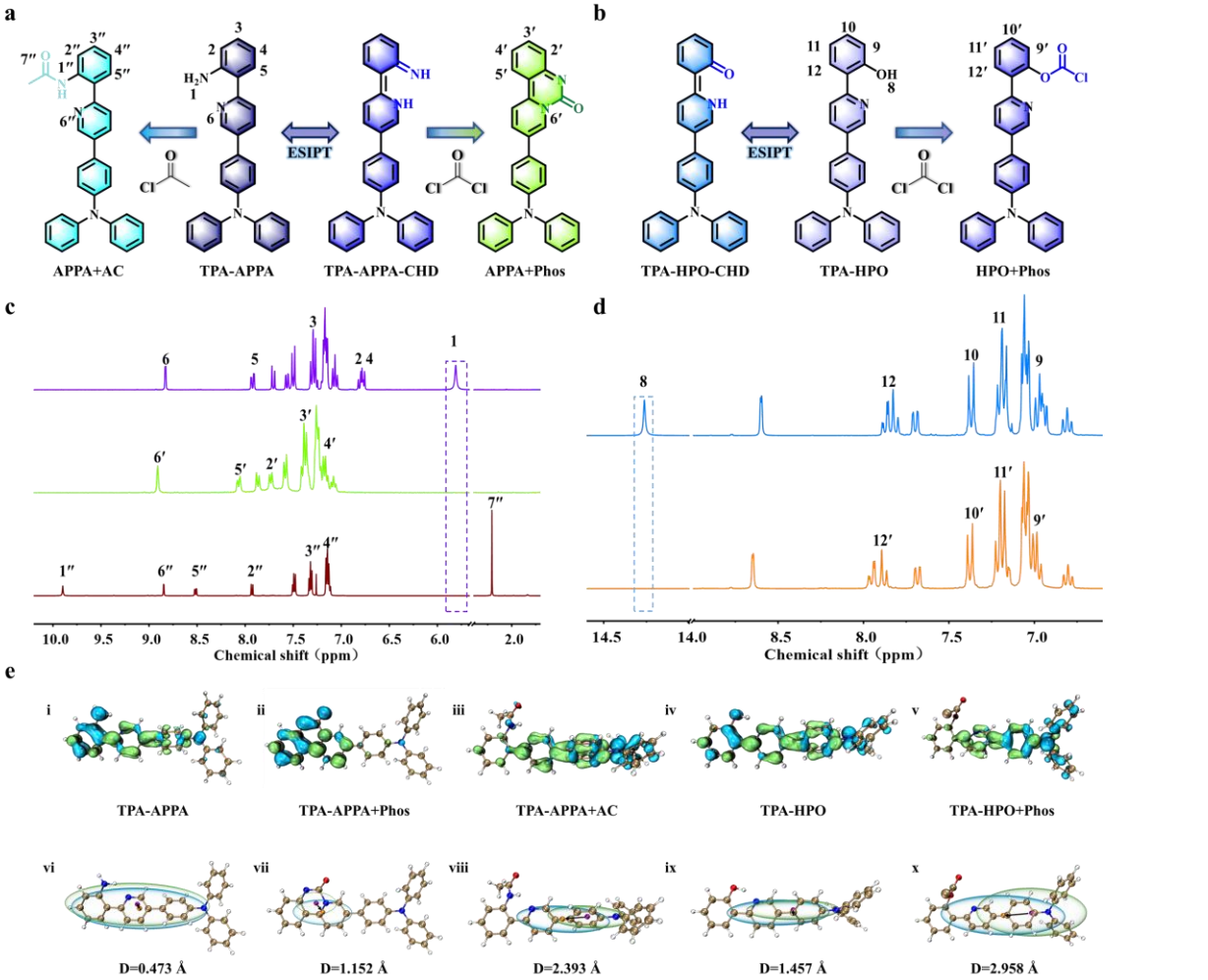

Figure 3. (a, b) Proposed working mechanism of **TPA-APPA** and **TPA-HPO**. (c) ^{1}H NMR spectra of **TPA-APPA**, **APPA+Phos**, and **APPA+AC** in deuterated chloroform; (d) ^{1}H NMR spectra of **TPA-HPO** and **HPO+Phos** in deuterated chloroform. (e) Hole-electron distribution analysis for the **TPA-APPA** and **TPA-HPO** probes and the products **APPA+Phos**, **APPA+AC**, and **HPO+Phos**: (i-v) hole and electron distributions; (vi-x) the $C_{hole}/C_{electron}$ plots smoothly derived from the hole and electron distributions, with the centroids of C_{hole} and $C_{electron}$ indicated by purple and orange spheres, respectively, and the charge transfer distances labeled as D.

Further analysis of the S_0 and S_1 energy distribution states of **TPA-APPA** and **TPA-HPO**, both prior to and following the reaction, revealed that the incorporation of carbonyl groups in the products **APPA+Phos**, **APPA+AC**, and **HPO+Phos** markedly increased the electron withdrawing capacity of these molecules. This modification stabilized their LUMO relative to those of the unreacted probes **TPA-APPA** and **TPA-HPO**, thereby resulting in a reduced energy gap. Specifically, for the probe **TPA-APPA** and its product **APPA+AC**, the vibronic intensity (f) increased from 1.0686 to 1.1283, indicating an enhancement in fluorescence intensity. Notably, although the calculated vibronic intensity of **APPA+Phos** (0.4562) is lower than that of **TPA-APPA** (1.0686), experimental measurements revealed a marked increase in fluorescence emission intensity. This discrepancy is attributed to structural changes after reaction, which are proposed to suppress nonradiative relaxation pathways, thereby increasing the fluorescence quantum yield and producing the observed enhancement (Figures S22 and S23).

Furthermore, hole-electron analysis demonstrated that the electron distributions of **TPA-APPA** and **TPA-HPO** were similar, with electrons predominantly localized on the benzene ring adjacent to the amino or hydroxyl substituents. In contrast, the holes were distributed across the benzene ring and the pyridine-containing segment of the benzene ring, indicative of LE characteristic (Figure 3e (i, iv)). Following the reaction, the electron density of **APPA+Phos** remained concentrated within the original donor region; however, the hole distribution shifted markedly toward the right side of the molecule. The introduction of phosgene resulted in a decrease in the molecule's LUMO energy level and a reduction in electron density within the connected region, thereby facilitating a preferential migration of excited state electrons from the donor region toward the vicinity of the ureido group (Figure 3e (ii)). In the case of **APPA+AC** with **HPO+Phos**, electrons were primarily localized in the triphenylamine moiety, likely attributable to the electron withdrawing effect of the acyl group introduced via the reaction

between AC and phosgene. This effect diminished the electron cloud density in the connected region, effectively redistributing electrons away from the acyl region toward the triphenylamine moiety, leading to an electron density biased toward this donor unit (Figure 3e (iii, vi). The alterations in electron distribution were also evidenced by changes in the centroid distance (D) of the hole (C_{hole}) and the electron ($C_{electron}$) before and after the reaction of the probes **TPA-APPA** and **TPA-HPO**. Specifically, the centroid distance of **TPA-APPA** increased from 0.473 Å to 1.152 Å and subsequently to 2.393 Å, while those of **TPA-HPO** increased from 1.457 Å to 2.958 Å. These changes indicate a pronounced intramolecular charge transfer process occurring in both probes (Figure 3e(vi–x)). These computational results further validate the recognition mechanisms of **TPA-HPO** and **TPA-APPA** for phosgene and AC, as well as their associated optical responses.

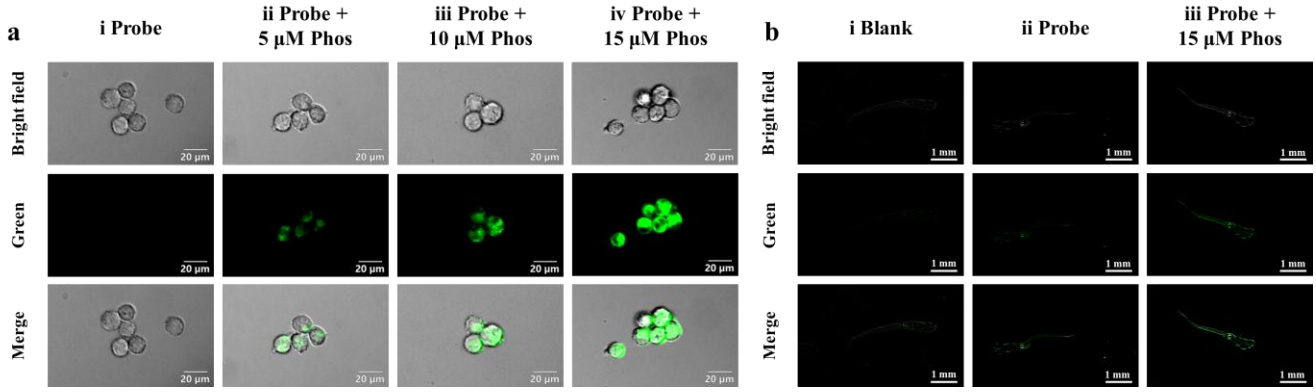

Figure 4. (a) Fluorescence images of HeLa cells incubated with 5 μM of probe **TPA-APPA** for 20 min: (i-iv) HeLa cells incubated with 5 μM of probe **TPA-APPA** for 20 min and further incubated with a 0-15 μM concentration gradient of triphosgene for another 20 min. Scale bar=20 μm. (b) Fluorescence images of zebrafish: (i-iii) Zebrafish incubated with 5 μM of probe **TPA-APPA** and further incubated with 15 μM of triphosgene for another 20 min. Green channel: λ_{em}=408-488 nm (λ_{ex}=516 nm). Scale bar=1 mm.

Cells and Zebrafish Imaging Studies. To assess the fluorescence response capability of the probe **TPA-APPA** toward intracellular phosgene in living cells, we first evaluated the toxicity of **TPA-APPA** by CCK-8 assay.[38] HeLa cells were incubated with **TPA-APPA** at various concentrations (0-20 μM) for 24 h. The results revealed that the cell survival rate was still more than 96% after incubation with probe up to 20 μM for 24 h, indicating low cytotoxicity and favorable biocompatibility of the probe (Figure S24). Based on these results, fluorescence imaging of exogenous phosgene in living cells was performed using confocal laser scanning microscopy. HeLa cells were first incubated with 5 μM **TPA-APPA** for 20 min, then treated with different concentrations of triphosgene (0-15 μM) for an additional 20 min. Because phosgene is highly toxic and undergoes rapid decomposition in aqueous PBS, triphosgene was used as a phosgene surrogate. A stock solution of triphosgene was prepared in dimethyl sulfoxide and subsequently diluted with PBS to the desired working concentrations prior to cell treatment. The cells were then washed three times with PBS to remove residual probe and triphosgene before imaging. A gradual increase in green channel fluorescence intensity was observed with increasing triphosgene concentration (Figure 4a). Quantitative analysis of fluorescence intensity using ImageJ revealed nearly a threefold increase in signal compared to the untreated control group (Figure S25). These findings demonstrate that **TPA-APPA** exhibits excellent cell permeability, low cytotoxicity, and high sensitivity to phosgene generated from triphosgene, underscoring its potential for live cell fluorescence imaging applications.

The above experiments confirmed the feasibility of using **TPA-APPA** for imaging exogenous phosgene in living cells, highlighting its potential in bioimaging applications. To further investigate it exogenous imaging performance, we selected zebrafish as a model organism due to their partial genetic homology with humans, optical transparency, and suitability for live imaging studies.[39] Zebrafish larvae were incubated with 5 μM **TPA-APPA** for 30 min. In the absence of exogenous triphosgene, no significant green fluorescence was observed, likely attributable to the absence of endogenous phosgene in zebrafish. In contrast, exposure to 15 μM triphosgene produced a pronounced fluorescence increase in the green channel, indicating that the probe could specifically respond to and visualize phosgene released in situ from triphosgene in a living organism (Figure 4b). These results further demonstrate the utility of **TPA-APPA** as a fluorescent probe for in vivo phosgene detection and imaging.

Effect of Substrate Materials on Adsorption Capacity and Gas Phase Sensing of Phosgene. The detection of phosgene in the gaseous phase is critically important for environmental safety. Given its excellent spectral response in solution, **TPA-APPA** was employed to fabricate test strips for the rapid, on-site detection of phosgene and AC vapors. Conventional test strips typically utilize either non-fluorescent filter paper or meltblown cloth as substrates. Filter paper is often preferred for its air permeability and flexibility, which make it suitable for field applications.[40-42] By contrast, meltblown cloth offers enhanced detection sensitivity owing to its high specific surface area and superior adsorption capacity.[25, 28] While ceramic fiber provides a large surface area and exhibits excellent thermal and chemical stability, making it highly suitable for gas sensing in harsh environments.

To identify the optimal substrate for **TPA-APPA** vapor detection, a comparative evaluation of the three materials was conducted (Figure 5a). Test strips prepared using non-fluorescent filter paper and loaded with **TPA-APPA** displayed weak blue fluorescence under 365 nm UV light. Upon 30 s of exposure to phosgene vapor, a visible color change from light gray to light yellow was observed under ambient light. Under UV light, the fluorescence intensified slightly, shifting from weak blue to light green. However, the extent of both visible and fluorescent color change was less pronounced compared to the other substrates (Figure S26). Under identical conditions, meltblown cloth-based test strips exhibited a more significant fluorescence enhancement under 365 nm UV light. A distinct fluorescence shift from blue to green was observed at approximately 5 ppm phosgene, with intensity increasing progressively with higher

concentrations, indicating a strong fluorescence response. Under visible light, the strips turned from colorless to yellowish, though this transition was relatively subtle (Figure S27). Notably, ceramic fiber test strips showed the most sensitive response. After 30 s of exposure to phosgene vapor, a visible color change from colorless to brownish yellow was observed. Under UV irradiation, fluorescence was significantly enhanced even at 2.5 ppm phosgene, with a color transition from weak blue to intense green (Figure S28 and S29).

To overcome the limitations of visual discrimination of subtle color changes, colorimetric signals were digitized in real time to enhance detection accuracy and reliability. Within the concentration range of 0-30 ppm for phosgene and AC, the ratios of the green to blue channels (G/B) exhibited strong linear correlations with the concentrations of phosgene (R^2=0.999) and AC (R^2=0.997), demonstrating the method's high potential for quantitative detection.

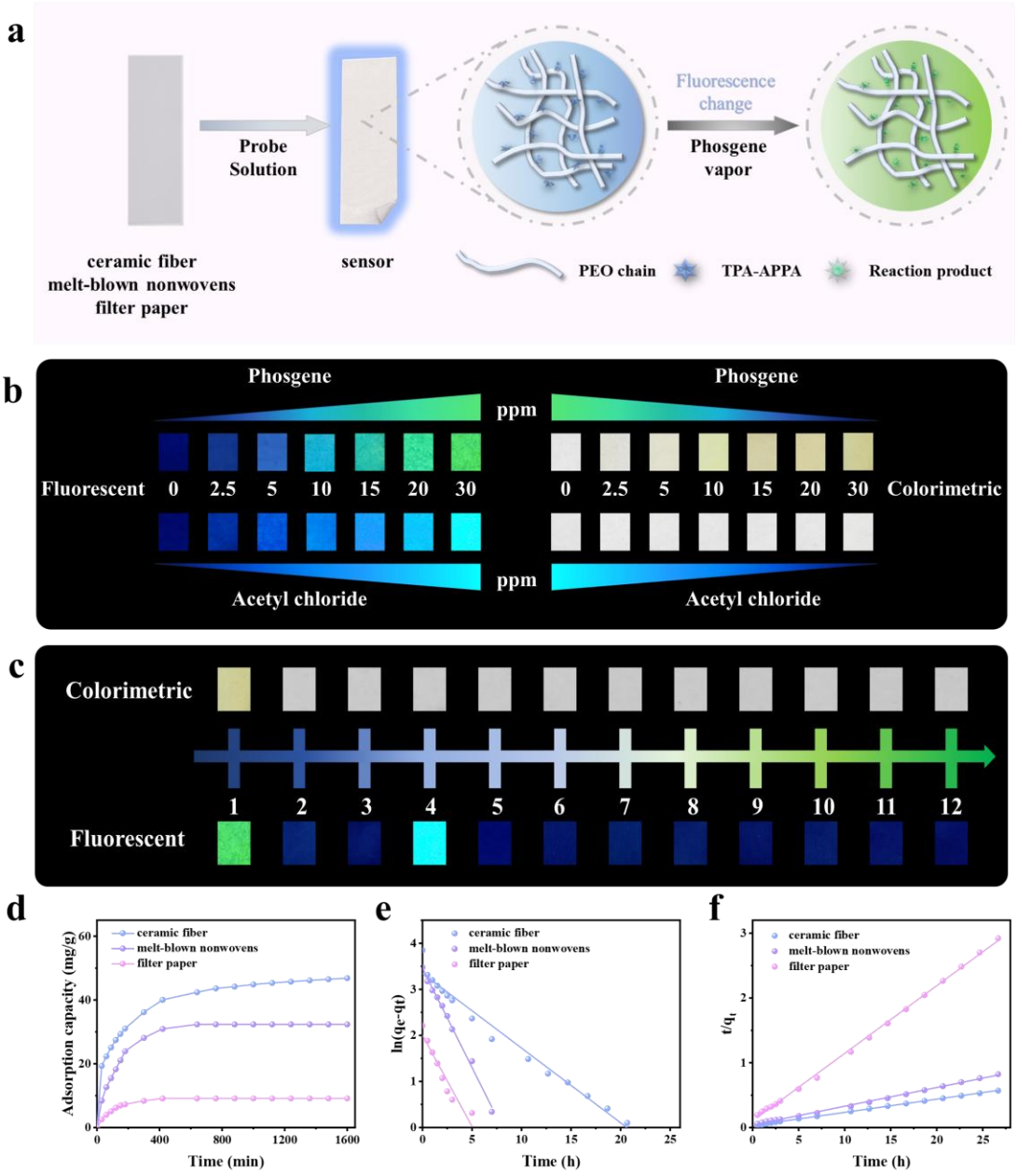

Figure 5. (a) Schematic illustration of the fabrication process for the **TPA-APPA** test strip. (b) Fluorescence images of **TPA-APPA** test strips before and after exposure to phosgene and AC vapors at concentrations ranging from 0-30 ppm at 24℃ and 30% relative humidity. (c) Fluorescence images of **TPA-APPA** test strips following exposure to 30 ppm phosgene, various nerve agent simulants, and AC. All fluorescence images were captured under illumination with a 365 nm lamp for the following substances: (1) phosgene, (2) TsCl, (3) $SOCl_2$, (4) AC, (5) $(COCl)_2$, (6) BzCl, (7) $POCl_3$, (8) FA, (9) Ben, (10) DCP, (11) DCNP, and (12) CEES at 24℃ and 30% relative humidity. (d) **TPA-APPA**-loaded ceramic fibers, meltblown cloth, and non-fluorescent filter paper utilized for the adsorption of triphosgene. (e) PFO model. (f) PSO model.

To evaluate the probe's response to other analytes, ceramic fiber test strips loaded with **TPA-APPA** were subsequently exposed to AC vapor, resulting in a pronounced enhancement of blue fluorescence (Figure 5b). This observation demonstrates the feasibility of dual mode detection for both phosgene and AC. In comparison, only phosgene induced a significant green

fluorescence response in the test strips after 2 min of exposure to 30 ppm phosgene vapor and other analytes. By contrast, AC produced a pronounced blue fluorescence response, while other phosphorus containing compounds elicited negligible fluorescence changes (Figure 5c). Furthermore, evaluating the interference resistance of the test strips is essential. Notably, although $SOCl_2$ alone produced negligible fluorescence changes, in the presence of phosgene it tended to increase the blue-channel signal, similar to AC. In particular, AC and $SOCl_2$ may compete with phosgene for nucleophilic sites or generate HCl, leading to acidification and partial quenching, which can impact the green fluorescence appearance. In the colorimetric mode, all treatment groups displayed comparable brownish-yellow hues, indicating that the interferents did not significantly affect the visual color response (Figure S30). Quantitatively, the image-derived indices $1\text{-}B/B_0$ (B and B_0 denote the blue-channel intensities after and before exposure, respectively) and G/B showed no significant deviation relative to phosgene alone (Figure S31). These results demonstrate the excellent selectivity and sensitivity of **TPA-APPA** modified ceramic fiber test strips for rapid detection of phosgene and AC.

To investigate how different substrate materials influence the detection performance and optical stability of the **TPA-APPA** probe, we constructed a custom adsorption system. This system was used to evaluate the adsorption capacities of **TPA-APPA**-loaded meltblown nonwoven fabric, non-fluorescent filter paper, and ceramic fiber toward triphosgene vapor. In the experimental setup, the three substrate-based composites were placed in a sealed sample chamber, and triphosgene vapor was introduced via an air pump. Adsorption performance was quantified by monitoring the mass change of the chamber over time. All three materials exhibited rapid adsorption during the first 300 min, followed by a slower increase as adsorption sites approached saturation. The meltblown cloth and non-fluorescent filter paper reached adsorption equilibrium at approximately 600 and 420 min, respectively (Figure 5d). Among the tested materials, ceramic fiber demonstrated the highest adsorption capacity of 46.8 mg g^{-1}, compared to 32.3 mg g^{-1} and 9.12 mg g^{-1} for meltblown cloth and filter paper, respectively. This superior performance is attributed to the larger pore structure and higher specific surface area of ceramic fiber, which facilitates the diffusion of triphosgene molecules to active sites.

To further analyze the adsorption kinetics, both pseudo first order (PFO) and pseudo second order (PSO) kinetic models were applied to the experimental data (Figures 5e and 5f). The R^2 values of the PFO model for ceramic fiber, melt-blown nonwovens, and filter paper were 0.994, 0.958, and 0.926, respectively, whereas those of the PSO model were 0.998, 0.999, and 0.998, respectively. The consistently higher correlation coefficients obtained with the PSO model indicate that the adsorption process is better described by a pseudo second order kinetic model, suggesting a chemisorption-controlled mechanism. In summary, ceramic fiber combines superior adsorption performance with excellent mechanical strength, thermal resistance, and chemical stability, making it the most suitable substrate for TPA-APPA based gas-phase detection.

Intelligent Recognition Based on CNNs and Swin Transformer. Convolutional Neural Networks (CNNs) represent an advanced classification approach for image analysis.[43, 44] In this study, we employ a CNN-based classifier to categorize gas concentration levels from fluorescence images of the test strips, allowing the network to learn chromatic features associated with concentration dependent signal changes. The CNN consists of stacked convolution ReLU blocks with periodic downsampling through max pooling, followed by a fully connected classification head.[45] This downsampling reduces spatial resolution and improves robustness to local perturbations such as noise and minor deformations. As depth increases, the number of feature filters is typically expanded to capture higher-level representations. Finally, the classification head maps the learned representation to the concentration-class space as K classes to produce the predicted concentration level. This approach enables accurate classification of phosgene and acetyl chloride concentrations for portable detection applications. Although CNNs are well suited to enhance detection accuracy, their inherent local receptive field limitations and network depth pose challenges in achieving high precision recognition of multi-category and fine-grained gas concentration images. This issue is particularly pronounced in scenarios involving complex background interference and subtle inter-sample differences, which significantly impair recognition accuracy.[46] Consequently, the feature representation capability of the CNNs is substantially challenged, yielding a validation accuracy of only 88.2% as demonstrated in experimental results (Figure 6a).

To address the limitations of CNNs, we propose the use of the Swin Transformer as the backbone architecture. This model effectively captures long-range dependencies within images while preserving local feature modeling through its hierarchical structure and sliding-window self-attention mechanism, thereby substantially enhancing overall recognition accuracy and robustness.[47, 48] Effective model training necessitates a large volume of data; however, acquiring extensive image datasets can be challenging. To mitigate this issue, we employ a data augmentation strategy to expand the dataset (Figure S32). Specifically, we apply diverse augmentation techniques across three categories: geometric transformations, optical property adjustments, and spectral property modifications. Geometric transformations include random rotation, cropping, scaling, and horizontal and vertical flipping.[49] Optical augmentations involve adjustments to brightness, contrast, and the application of Gaussian blur. Spectral augmentations encompass hue fine tuning, color dithering, and random channel replacement. These augmentation methods simulate a wide range of realistic image variations from a limited set of original images, thereby addressing dataset scarcity and enhancing the model's generalization capabilities.[50]

The segmentation module divides the input image into *N* equally sized small segments. Subsequently, self-attention computations are performed independently within each segment. To facilitate information exchange between windows, a sliding window technique is employed, wherein the window positions are shifted between consecutive Transformer layers to enhance inter window connectivity. To further extract multi-scale features, the feature maps are down sampled using the Patch Merging module, which reduces the width and height of the feature maps by half while doubling their depth. Through this hierarchical structure, local and global features are progressively integrated to produce the final feature vector. Following the initial feature extraction, the image features are represented as increasingly abstract, high-level feature maps. Once these feature maps are obtained, specific training and concentration classification tasks can be conducted (Figures 6b and 6c).

After feature-map extraction, the model was trained to classify gas concentration levels. In this study, we selected the Swin Transformer as the backbone network for experimental validation. All input images were resized to 224×224 pixels and

partitioned into 4×4 patches via patch embedding. The network comprises four hierarchical stages with channel dimensions of 96, 192, 384, and 768, enabling progressive multi-scale feature representation. During training, model parameters were optimized using the Adam optimizer, and cross-entropy loss was adopted for the gas-concentration classification task. The initial learning rate was set to 1×10^{-4} and was dynamically adjusted using a cosine decay schedule to ensure stable convergence. The batch size and total number of training epochs were set to 16 and 100, respectively. To ensure a fair comparison across models, the dataset was split into 80% for training and 20% for validation. In addition, dropout (0.2) and weight decay (0.05) were introduced as regularization strategies to mitigate overfitting under limited-sample conditions.

We first evaluated the Swin Transformer on the original dataset without augmentation, achieving a validation accuracy of only 70.6%. After applying data augmentation, the validation accuracy markedly increased to 98.0%. To ensure a fair baseline comparison, we constructed a conventional CNN model with a comparable structural complexity and parameter scale, and trained it under the same data augmentation protocol. Although the CNN also benefited from augmentation, its best validation accuracy reached only 80.2%, which remained substantially lower than the 98.0% achieved by the Swin Transformer. These results indicate that, even under identical augmentation settings, the CNN has limited capacity to model the discriminative features in fluorescence images, whereas the Swin Transformer more effectively captures multi-scale representations and long-range dependencies, leading to superior performance in this task.

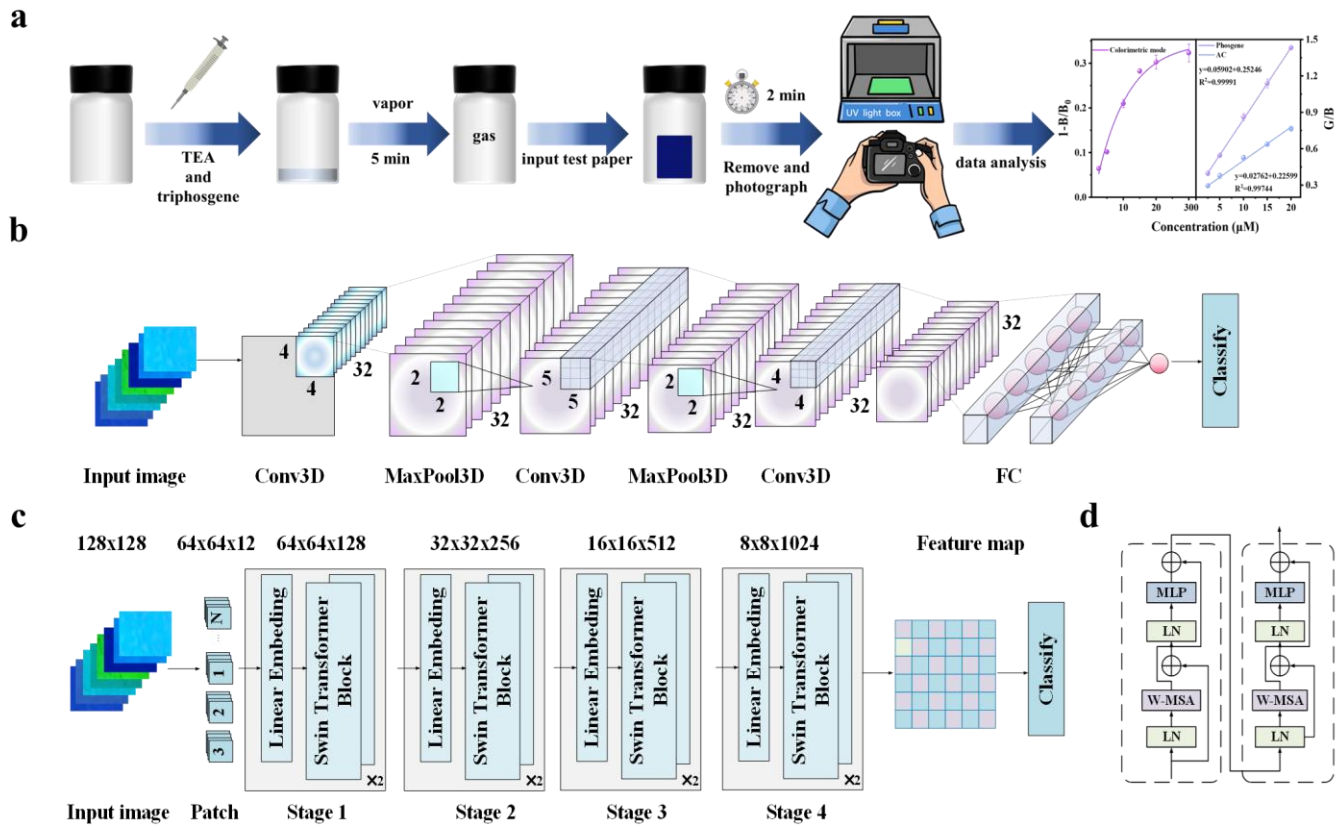

Figure 6. (a) Schematic diagram of phosgene vapor determined by **TPA-APPA** test strips. (b) Flowchart illustrating gas image classification using CNN. (c) Flowchart depicting gas detection classification employing the Swin Transformer. (d) Attention mechanism block of the Swin Transformer.

CONCLUSIONS

In summary, we developed two fluorescent probes, **TPA-HPO** and **TPA-APPA**, by integrating ESIPT and HLCT mechanisms to achieve enhanced sensitivity and selectivity toward reactive phosgene and acetyl chloride. The resulting probe system effectively minimizes interference from protonic acids during detection, thereby ensuring reliable fluorescence signaling in complex environments. Among them, **TPA-APPA** exhibited ultrasensitive and ratiometric fluorescence responses to phosgene, along with excellent biocompatibility for real time imaging in cells and zebrafish. Furthermore, its incorporation into portable test strips, together with deep learning–assisted image classification, indicates potential for smart, field-deployable toxic gas detection. This work bridges molecular probe design, materials integration, and machine learning driven analytics, offering insights for next-generation optical sensors and hazardous chemical monitoring; notably, the AI module exhibited robust classification performance even when trained on limited datasets.

ASSOCIATED CONTENT

Supporting Information

Additional experimental details, NMR and HRMS spectra, and other supporting figures.

AUTHOR INFORMATION

Corresponding Author

Xiaobai Li - College of Chemistry, Chemical Engineering and Resource Utilization, Northeast Forestry University, Harbin, 150040, China; E-mail: lixiaobai2008@126.com.
Yongpeng Liu - Yusuf Hamied Department of Chemistry, University of Cambridge, Cambridge CB2 1EW, UK; E-mail: yl862@cam.ac.uk. Institute of Applied Physics and Materials Engineering, University of Macau, Avenida da Universidade, Taipa, Macau 999078, China. E-mail: ypliu@um.edu.mo.
Shilong Yang - Heilongjiang Key Laboratory of Complex Traits and Protein Machines in Organisms, Northeast Forestry University, Harbin 150040, China; E-mail: syang2020@nefu.edu.cn.
Hongwei Ma - Heilongjiang Key Laboratory of Complex Traits and Protein Machines in Organisms, Northeast Forestry University, Harbin, 150040, China; E-mail: mahw@nefu.edu.cn.

Notes:

The authors declare no competing financial interest.

ACKNOWLEDGMENT

We are grateful for the financial supported by the National Key R&D Program of China (2023YFF1304903), National Natural Science Foundation of China (22374017; 22576031), Fundamental Research Funds for the Central Universities (2572025JT07), the Natural Science Foundation of Heilongjiang Province (2024ZXDXC28).

REFERENCES

(1) Boyland, E., Biochemical Reactions of Chemical Warfare Agents. *Nature.* **1948**, *161* (4085), 225-227.
(2) Kumar, S. M.;Munusamy, S.;Manickam, S.;Jothi, D.;Enbanathan, S.;Iyer, S. K., Ratiometric detection of lethal oxalyl and thionyl chloride by a thiophene-appended phenanthridine sensor, *J. Mol. Liq.* **2024**, *415*, 126388.
(3) Meng, W.-Q.;Sedgwick, A. C.;Kwon, N.;Sun, M.;Xiao, K.;He, X.-P.;Anslyn, E. V.;James, T. D.;Yoon, J., Fluorescent probes for the detection of chemical warfare agents. *Chem. Soc. Rev.* **2023**, *52* (2), 601-662.
(4) Zhang, L.;Song, K.;Liu, G.;Li, X.;He, Y.;Meng, Y.;Yang, Y.;Gong, T.;Wang, H.;Sun, K.;Zeng, L.;Yang, S.;Ma, H., Solid-state fluorescent films for detection of chemical warfare agents: Mechanisms, film engineering and integration with machine learning. *Coord. Chem. Rev.* **2025**, *540*, 216766.
(5) Babad, H.;Zeiler, A. G., Chemistry of phosgene. *Chem. Rev.* **1973**, *73* (1), 75-91.
(6) Tsuda, A., In situ photo-on-demand phosgenation reactions with chloroform for syntheses of polycarbonates and polyurethanes. *Polym. J.* **2023**, *55* (9), 903-912.
(7) Black, R. M.;Clarke, R. J.;Read, R. W.;Reid, M. T. J., Application of gas chromatography-mass spectrometry and gas chromatography-tandem mass spectrometry to the analysis of chemical warfare samples, found to contain residues of the nerve agent sarin, sulphur mustard and their degradation products. *J. Chromatogr. A.* **1994**, *662* (2), 301-321.
(8) Jeltes, R.;Burghardt, E.;Breman, J., Gas chromatographic determination of phosgene and dichloroacetylene in air. *Occup. Environ. Med.* **1971**, *28* (1), 96.
(9) Liu, G.;Lin, Y., Electrochemical Sensor for Organophosphate Pesticides and Nerve Agents Using Zirconia Nanoparticles as Selective Sorbents. *Anal Chem.* **2005**, *77* (18), 5894-5901.
(10) Bissinger, J. M.;Rullo, K. T.;Stoklosa, J. T.;Shearer, C. M.;DeAngelis, N. J., High-performance liquid chromatographic analysis of acid chlorides by pro-derivatization. *J. Chromatogr. A.* **1983**, *268*, 102-106.
(11) Cheng, H.-B.;Li, Y.;Tang, B. Z.;Yoon, J., Assembly strategies of organic-based imaging agents for fluorescence and photoacoustic bioimaging applications. *Chem. Soc. Rev.* **2020**, *49* (1), 21-31.
(12) Zhang, H.; Rudkevich, D. M. A FRET Approach to Phosgene Detection. *Chem. Commun.* **2007**, *12*, 1238.
(13) Zhu, B.; Yang, X.; Jiang, L.; Chen, T.; Wang, S.; Zeng, L. A Portable and Versatile Fluorescent Platform for High-Throughput Screening of Toxic Phosgene, Diethyl Chlorophosphate and Volatile Acyl Chlorides.*Chin. Chem. Lett.* **2025**, *36* (1), 110222.
(14) Ji, M.; Ding, N.; Jiang, Y.; Gou, X.; Lin, S.; Zhou, J.; Peng, L.; Peng, H.; Fang, Y. Selective Phosgene Detection Both in Solution and Gas Phases via a Unique Fluorescence Bright-off-Brighter Mechanism. *Sens. Actuators, B.* **2025**, *426*, 137115.
(15) Chen, L.; Wu, D.; Kim, J.-M.; Yoon, J. An ESIPT-Based Fluorescence Probe for Colorimetric, Ratiometric, and Selective Detection of Phosgene in Solutions and the Gas Phase. *Anal. Chem.* **2017**, *89* (22), 12596-12601.
(16) Shao, S.; Bao, C.; Zhou, B.; Han, Y. A Novel Benzo Hemicyanine-Based Fluorescent Probe for Susceptible Visualizing Detection of Phosgene. *Talanta.* **2023**, *265*, 124912.
(17) Mo, W.; Zhu, Z.; Kong, F.; Li, X.; Chen, Y.; Liu, H.; Cheng, Z.; Ma, H.; Li, B. Controllable Synthesis of Conjugated Microporous Polymer Films for Ultrasensitive Detection of Chemical Warfare Agents. *Nat. Commun.* **2022**, *13* (1), 5189.
(18) Li, X.; Lv, Y.; Chang, S.; Liu, H.; Mo, W.; Ma, H.; Zhou, C.; Zhang, S.; Yang, B. Visualization of Ultrasensitive and Recyclable Dual-Channel Fluorescence Sensors for Chemical Warfare Agents Based on the State Dehybridization of Hybrid Locally Excited and Charge Transfer Materials. *Anal. Chem.* **2019**, *91* (17), 10927-10931.
(19) Wang, K.; Hu, R.; Wang, J.; Zhang, J.; Liu, J.; Zhou, L.; Zhou, L.; Li, B. Fine Tuning the Energetics of 2-(2′-Hydroxyphenyl)Oxazoles to Obtain Highly Efficient Organic White-Light-Emitting Devices. *ACS Mater. Lett.* **2022**, *4* (11), 2337-2344.
(20) Li, Z.; Zhou, Z.; Yang, K.; Yao, Y.; Zhai, Y.; Wang, D.; Zeng, Z. Dual-Channel Deep-NIR-Emissive N-Embedded PAHs with Hybridized Local and Charge-Transfer Excited-State. *Chem. Sci.* **2025**, *16* (36), 16792-16800.
(21) Zhong, D.; Zhu, R.; Zhang, J.; Tao, P.; Su, B.; Yang, X.; Sun, Y.; Yue, L.; Zhou, G.; Wong, W.-Y. High-Efficiency Non-Doped near-Ultraviolet OLEDs Achieved by Regulating Excited-State Spatial Distribution through Molecular Optimization to Realize Hybridized Local and Charge-Transfer (HLCT) Characteristics. *Chem. Sci.* **2025**, *16* (37), 17156-17164.
(22) Zhu, Z.; Song, K.; Li, X.; Chen, Y.; Kong, F.; Mo, W.; Cheng, Z.; Yang, S.; Ma, H. A Wireless Fluorescent Sensing Device for On-Site Closed-Loop Detection of Hydrazine Levels in the Environment.*J. Hazard. Mater.* **2024**, *468*, 133809.
(23) Pumphrey, A. L.; Dong, H.; Driver, T. G. RhII2-Catalyzed Synthesis of A-, B-, or δ-Carbolines from Aryl Azides.*Angew. Chem., Int. Ed.* **2012**, *51* (24), 5920-5923.
(24) Lee, E.; Hooker, J. M.; Ritter, T. Nickel-Mediated Oxidative Fluorination for PET with Aqueous [^{18}F] Fluoride. *J. Am. Chem. Soc.* **2012**, *134* (42), 17456-17458.
(25) Zeng, L.; Chen, T.; Zhu, B.; Koo, S.; Tang, Y.; Lin, W.; James, T. D.; Kim, J. S. A Molecular Recognition Platform for the Simultaneous Sensing of Diverse Chemical Weapons. *Chem. Sci.* **2022**, *13* (16), 4523-4532.
(26) Zeng, L.; Zeng, H.; Jiang, L.; Wang, S.; Hou, J.-T.; Yoon, J. A Single Fluorescent Chemosensor for Simultaneous Discriminative Detection of Gaseous Phosgene and a Nerve Agent Mimic. *Anal. Chem.* **2019**, *91* (18), 12070-12076.
(27) Wang, S.-L.; Li, C.; Song, Q.-H. Fluorescent Chemosensor for Dual-Channel Discrimination between Phosgene and Triphosgene. *Anal. Chem.* **2019**, *91* (9), 5690-5697.
(28) Feng, W.; Liu, X.-J.; Xue, M.-J.; Song, Q.-H. Bifunctional Fluorescent Probes for the Detection of Mustard Gas and Phosgene.*Anal Chem.* **2023**, *95*, 1755-1763.
(29) Chen, G.; Zhou, W.; Zhao, C.; Liu, Y.; Chen, T.; Li, Y.; Tang, B. Rationally Optimized Fluorescent Probe for Imaging Mitochondrial SO_2 in HeLa Cells and Zebrafish. *Anal. Chem.* **2018**, *90* (21), 12442-12448.
(30) Kim, T.-I.; Hwang, B.; Bouffard, J.; Kim, Y. Instantaneous Colorimetric and Fluorogenic Detection of Phosgene with a Meso-Oxime-BODIPY. *Anal. Chem.* **2017**, *89* (23), 12837-12842.
(31) Mao, P.; Song, Y.; Zhao, X.; Wu, W.; Wang, Y. A Ratiometric Ben

zimidazole-Based Fluorescent Probe for The Recognition of Phosgene in Solution and Gaseous Phases. *J. Fluoresc.* **2024**, *35* (6), 3789-3797.
(32) Zeng, L.; Zeng, H.; Wang, S.; Wang, S.; Hou, J.-T.; Yoon, J. A Paper-Based Chemosensor for Highly Specific, Ultrasensitive, and Instantaneous Visual Detection of Toxic Phosgene. *Chem. Commun.* **2019**, *55* (91), 13753-13756.
(33) Wang, D.; Zhang, M.; Zhu, Q.; Adhikari, B. Intelligent Vegetable Freshness Monitoring System Developed by Integrating Eco-Friendly Fluorescent Sensor Arrays with Deep Convolutional Neural Networks. *Chem. Eng. J.* **2024**, *488*, 150739.
(34) Kong, F.; Yang, S.; Liao, X.; Feng, Z.; Shen, W.; Jiang, Z.; Zhou, D.; Zheng, Y.; Liao, L. Highly Efficient Sensitized Chiral Hybridized Local and Charge-Transfer Emitter Circularly Polarized Electroluminescence.*Adv. Funct. Mater.* **2022**, *32* (31), 2201512.
(35) Lippert, E. Spektroskopische Bestimmung Des Dipolmomentes Aromatischer Verbindungen Im Ersten Angeregten Singulettzustand.*Zeitschrift für Elektrochemie, Berichte der Bunsengesellschaft für physikalische Chemie.* **1957**, *61* (8), 962-975.
(36) Kwon, J. E.; Park, S. Y. Advanced Organic Optoelectronic Materials: Harnessing Excited-State Intramolecular Proton Transfer (ESIPT) Process.*Adv. Mater.* **2011**, *23* (32), 3615-3642.
(37) Lu, T.; Chen, Q. Independent Gradient Model Based on Hirshfeld Partition: A New Method for Visual Study of Interactions in Chemical Systems.*J. Comput. Chem.* **2022**, *43* (8), 539-555.
(38) Bao, K.; Li, Y.; Wei, J.; Li, R.; Yang, J.; Shi, J.; Li, B.; Zhu, J.; Mao, F.; Jia, R.; Li, J. Fangchinoline Suppresses Conjunctival Melanoma by Directly Binding FUBP2 and Inhibiting the Homologous Recombination Pathway. *Cell. Death. Dis.* **2021**, *12* (4), 380.
(39) Wu, W.-N.; Mao, P.-D.; Song, Y.-F.; Zhao, X.-L.; Wang, Y.; Xu, Z.-H. A Simple AIE-Based Indole-Benzimidazole Probe for the Ratiometric Fluorescent Detection of Phosgene in an Almost Neat Aqueous Solution. *Talanta.* **2025**, *283*, 127172.
(40) Liu, W.; Lv, K.; Lu, C.; Miao, X.; Zhao, C.; Li, F.; Zhang, M. Precise Intramolecular-Charge-Transfer Property Modulation of D-A-Type Fluorescent Probes for Bifunctional Detection of Phosgene and Nerve Agent.*Chem. Eng. J.* **2024**, *498*, 155457.
(41) Hu, Q.; Gong, T.; Mao, Y.; Yin, Q.; Wang, Y.; Wang, H. Two-Phase Activated Colorimetric and Ratiometric Fluorescent Sensor for Visual Detection of Phosgene via AIE Coupled TICT Processes. Spectrochim. *Acta. A. Mol. Biomol. Spectrosc.* **2021**, *253*, 119589.
(42) Xu, Z.; Luo, Y.; Hong, Y.; Liu, Z.; Zhang, M.-X.; Gu, S.-X.; Yin, J. A Naphthimide-Based Ratiometric Fluorescent Probe for Selective and Visual Detection of Phosgene in Solution and the Gas Phase. *Spectrochim. Acta. A. Mol. Biomol. Spectrosc.* **2022**, *269*, 120789.
(43) Pinckaers, H.;Ginneken, B. v.;Litjens, G. Streaming Convolutional Neural Networks for End-to-End Learning With Multi-Megapixel Images. *IEEE Trans. Pattern Anal. Mach. Intell.* **2022**, *44*, (3), 1581-1590.
(44) Zhao, H.; Liu, Y.; Li, G.; Lei, D.; Du, Y.; Li, Y.; Tang, H.; Dou, X. Electrophilicity Modulation for Sub-ppm Visualization and Discrimination of EDA.*Adv. Sci.* **2024**, *11* (18), 2400361.
(45) Jang, H., Tong, F. Improved modeling of human vision by incorporating robustness to blur in convolutional neural networks. *Nat. Commun.* **2024**, *15* (1), 1989.
(46) M. Luo, T. Xu, S. Xiao, H. K. Tsang, C. Shu, C. Meta-Optics Based Parallel Convolutional Processing for Neural Network Accelerator. *Laser Photonics Rev.* **2024**, *18*, 2300984.
(47) Liu, Z.; Lin, Y.; Cao, Y.; Hu, H.; Wei, Y.; Zhang, Z.; Lin, S.; Guo, B. Swin Transformer: Hierarchical Vision Transformer Using Shifted Windows. *arXiv:* 2103.140301989.
(48) Farooque, G.; Liu, Q.; Sargano, A. B.; Xiao, L. Swin Transformer with Multiscale 3D Atrous Convolution for Hyperspectral Image Classification. *Eng. Appl. Artif. Intell.* **2023**, *126* , 107070.
(49) Ranjbar, I.; Ventikos, Y.; Arashpour, M. Deep Learning-Based Construction and Demolition Plastic Waste Classification by Resin Type Using RGB Images. *Resour. Conserv. Recycl.* **2025**, *212*, 107937.
(50) L. Yang, C. Zhang, G. Liu, Z. Zhong and Y. Li. A Model for Robot Grasping: Integrating Transformer and CNN With RGB-D Fusion. *IEEE Trans. Consum. Electron.* **2024**, *70* (2), 4673-4684.

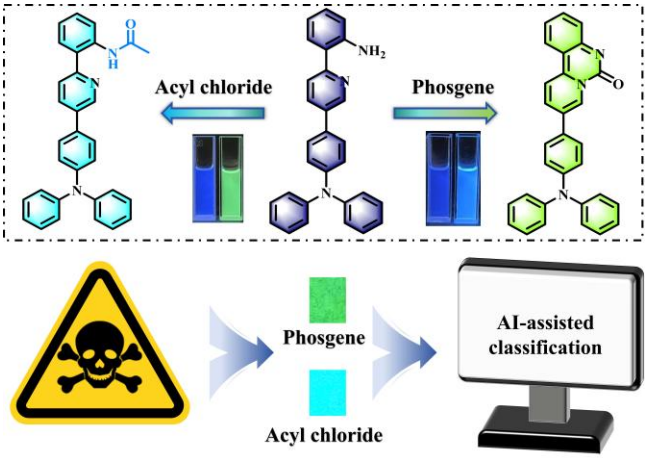

TOC